SESSION C: PRODUCTION TECHNOLOGIES, CAE AND MANAGEMENT

Three-objective Pareto optimization of GMAW process parameters using a modified force balance model

Mladen Rasinac[1*], Mišo Bjelić[1], Tanja Dulović[1], Jovana Perić[1], Marina Ivanović[1]

[1] University of Kragujevac, Faculty of Mechanical and Civil Engineering, Kraljevo, Serbia

ARTICLE INFO

[*] **Correspondence:** rasinac.m@mfkv.kg.ac.rs

DOI: https://doi.org/10.46793/ET26.C04R **PAGES:** C25 – C35

ABSTRACT

In this paper, a three-objective optimization model was developed for the preliminary selection of welding current and electrode wire extension length in the gas metal arc welding (GMAW) process, to achieve a droplet size characteristic for the projected spray metal transfer mode. The model is based on a modified force balance model, i.e., the MFBM approach, in which the droplet detachment condition is determined from the balance between the total detaching force and the surface tension force. A correction of the effective electrode wire neck radius, based on the balance between the pressure due to surface tension and the electromagnetic pinch pressure, was introduced to account for the tapering/necking effect at higher current values. The optimization variables are the welding current and electrode wire extension length, while the objective functions are defined to maximize the melting rate, minimize the deviation of the normalized droplet diameter from the target value, and minimize the normalized Joule/stick-out index. The obtained Pareto front indicates a clear compromise between productivity, droplet size control, and thermal loading of the electrode wire extension. A dynamic diagnostic layer was also introduced to verify the regularity of the droplet growth and detachment cycle for selected Pareto solutions.

KEYWORDS

GMAW, Metal transfer, MFBM, Pareto optimization, Projected spray transfer, Electrode wire neck radius

1. INTRODUCTION

Gas metal arc welding (GMAW) is one of the most widely used arc welding processes due to its high productivity, automation capability, and continuous feeding of filler material. The stability of this process largely depends on the mode of transfer of molten metal from the electrode wire tip to the weld pool. The metal transfer mode affects arc stability, spatter formation, weld bead geometry, penetration, and the overall quality of the welded joint [1-3]. Kim and Eagar showed that different transfer modes have different effects on arc stability, penetration, spatter, and weld bead quality, while Węglowski et al. discussed droplet size, transfer frequency, and droplet kinematics in the GMAW process.

In the GMAW process, the short-circuiting, globular, and spray metal transfer modes are most commonly considered. A particularly important region between the globular and spray modes is projected spray transfer, in which the droplets are approximately spherical, and their diameter may be approximately equal to or slightly larger than the electrode wire diameter. This mode is technologically interesting because it provides more stable metal transfer and less spatter compared with the globular mode, while at the same time representing a transitional region that may offer a more favorable compromise between transfer stability, productivity, and the thermal loading of the electrode wire compared with modes that require higher current values. However, projected spray transfer occurs within a relatively narrow range of welding parameters [1], [4].

For the preliminary selection of welding parameters, models based on the balance of forces acting on the droplet are useful. The classical static force balance model (SFBM) takes into account gravitational, electromagnetic, drag, and surface tension forces, whereas the modified force balance model, i.e., the MFBM model, additionally includes the force due to the momentum flux effect. Therefore, the MFBM model is suitable for estimating droplet size and detachment frequency in the globular and projected spray regions [4]. On the other hand, lumped-parameter dynamic models enable additional analysis of droplet growth, oscillation, and detachment [5], while models that include tapering and necking effects indicate the importance of changes in the electrode wire tip geometry at higher currents [6].

The aim of this paper is to develop a numerically efficient three-objective optimization model for selecting the welding current and electrode wire extension length in the GMAW process. The model is based on the MFBM approach, with a pressure-balance correction of the effective electrode wire neck radius. The optimization variables are the welding current I and electrode wire extension length l_e, while the optimization is formulated as a three-objective Pareto problem. A dynamic diagnostic layer is additionally used for verification of selected Pareto solutions.

2. MODEL AND OPTIMIZATION PROCEDURE

2.1. Modified Force Balance Model

In this paper, the droplet detachment condition was described using the MFBM model. Immediately before detachment, the droplet is approximated by a spherical shape, while detachment is defined by comparing the total detaching force F_T and the surface tension force. The total force acting on the droplet is given by [4]:

$$F_T = F_g + F_{em} + F_d + F_{mf} \tag{1}$$

where F_g denotes the gravitational force, F_{em} the electromagnetic force, F_d the drag force exerted by the shielding gas or plasma, and F_{mf} the force resulting from the momentum flux effect. The droplet detachment condition can be written as:

$$F_T \geq F_s \tag{2}$$

where F_s denotes the surface tension force that retains the droplet at the electrode wire tip. The classical force balance model (SFBM) considers gravitational, electromagnetic, drag, and surface tension forces, whereas the MFBM model additionally includes the force F_{mf}. The inclusion of F_{mf} represents the main difference between the MFBM and the classical force balance model.

A schematic representation of the forces acting on the molten droplet and the corresponding lumped-parameter dynamic analogy is shown in Figure 1.

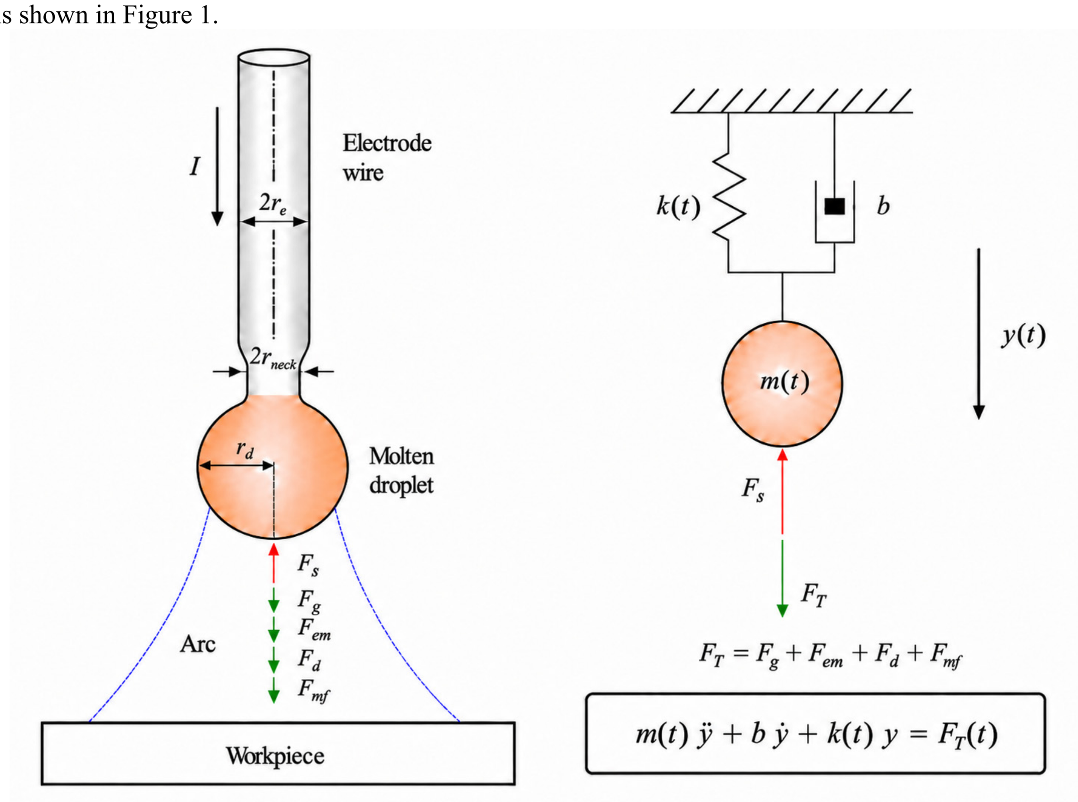

Figure 1: Forces acting on the droplet and dynamic MFBM analogy

The droplet radius is defined as:

$$r_d = \frac{D}{2} \tag{3}$$

where D is the current droplet diameter. Assuming a spherical droplet shape, the droplet mass is calculated from the expression:

$$m_d = \frac{4}{3}\pi\rho_e r_d^3 \tag{4}$$

where ρ_e is the density of the molten electrode wire metal. The gravitational force is then:

$$F_g = m_d g \tag{5}$$

where g is the gravitational acceleration.

The electromagnetic force in the MFBM model is calculated according to the expression:

$$F_{em} = \frac{\mu_0 I^2}{4\pi}\left[\ln\left(\frac{r_d \sin\theta}{r_e}\right) - \frac{1}{4} - \frac{1}{1-\cos\theta} + \frac{2}{(1-\cos\theta)^2}\ln\left(\frac{2}{1+\cos\theta}\right)\right] \tag{6}$$

where μ_0 is the magnetic permeability of vacuum, r_e is the electrode wire radius, and θ is the angle of the droplet surface region covered by the arc. In this paper, for the argon-rich shielding atmosphere, $\theta = \pi/2$ was adopted [4].

The shielding gas or plasma drag force is determined by the expression:

$$F_d = \frac{1}{2} C_d A_d \rho_p v_p^2 \tag{7}$$

where C_d is the drag coefficient, A_d is the effective droplet area exposed to the flow, ρ_p is the density of the plasma or shielding gas, and v_p is the characteristic flow velocity. The effective droplet area exposed to the flow is calculated as:

$$A_d = \pi(r_d^2 - r_e^2) \tag{8}$$

To define the momentum flux force, the following dimensionless ratio is introduced $\alpha = r_d/r_e$.

For argon-rich shielding gases, the momentum flux force is calculated as:

$$F_{mf} = \frac{\mu_0 I^2}{4\pi}\left[\frac{1}{\alpha^2} - \left(1 - \sqrt{1 - \frac{1}{\alpha^2}}\right)^2\right] \tag{9}$$

where $\alpha \geq 1$ [4].

The surface tension force in the classical MFBM model takes the form:

$$F_s = 2\pi r_e \gamma \tag{10}$$

where γ is the surface tension of the molten metal. In this paper, due to the inclusion of the tapering/necking effect, the electrode wire radius r_e in the expression for the surface tension force is replaced by the effective neck radius r_{neck}. Therefore, in the developed model, the following is used [6]:

$$F_s = 2\pi r_{neck} \gamma \tag{11}$$

This equation represents the link between the MFBM model and the introduced pressure-balance correction of the e-lectrode tip geometry. It is important to emphasize that the electromagnetic force and the momentum flux force remain in the Anzehaee/Haeri form, while the effective neck radius is used only in the surface tension force.

2.2. Pressure-Balance Correction of the Effective Neck Radius

At higher current values, a more pronounced electromagnetic action occurs in the electrode tip region, which may cause a reduction in the effective droplet neck. To take this effect into account, the effective neck radius r_{neck} is introduced. This approach is inspired by the work of Kang and Chung, in which the influence of the tapering effect and the necking region on the dynamic detachment of a droplet in the GMAW process is considered [6].

The raw value of the effective neck radius is determined from the equilibrium condition between the pressure due to surface tension and the electromagnetic pinch pressure [6]:

$$r_{neck,raw} = \frac{8\pi^2 \gamma r_e^2}{\mu_0 I^2} \tag{12}$$

Since the effective neck radius cannot be greater than the electrode wire radius, an upper bound is introduced:

$$r_{neck} \leq r_e \tag{13}$$

Additionally, for numerical stability and to avoid a physically unrealistic small neck radius, a lower bound is introduced:

$$r_{neck} \geq \eta_{min} r_e \tag{14}$$

where the following value is adopted in this paper: $\eta_{min} = 0.30$.

The final expression for the effective neck radius is:

$$r_{neck} = \max\left[\eta_{min} r_e, \min\left(r_e, \frac{8\pi^2 \gamma r_e^2}{\mu_0 I^2}\right)\right] \tag{15}$$

The critical current at which the effective neck radius begins to decrease is obtained from the condition $r_{neck,raw} = r_e$, i.e.:

$$I_{crit} = \sqrt{\frac{8\pi^2 \gamma r_e}{\mu_0}} \tag{16}$$

For the model parameters used, the following value was obtained: $I_{crit} = 221.4$ A.

In this paper, the complete Kang-Chung neck rupture criterion is not used; instead, the tapering/necking effect is introduced through a correction of the surface tension force within the MFBM detachment condition. In other words, droplet detachment is still determined according to the condition (2), while the geometrical effect of the neck is taken into account through the effective radius r_{neck}. This limitation is important because the developed model remains within the framework of a numerically simple MFBM approach and does not transition into a complete dynamic model of neck rupture.

2.3. Estimation of Droplet Diameter and Detachment Frequency

The electrode melting rate is described by the expression [4,5], [7]:

$$MR = c_1 I + c_2 \rho_{res} I^2 l_e \tag{17}$$

where MR is the volumetric melting rate, ρ_{res} is the linear electrical resistance, and c_1, c_2, are model coefficients. The first term describes the contribution associated with the current and heating in the arc region, while the second term describes the contribution of resistive, i.e., Joule heating of the electrode wire extension. Similar expressions for the melting rate and its importance in the modelling and control of the GMAW process are discussed in the works of Ersoy et al. and Thomsen [5], [7]. The mass flow rate of the molten metal is calculated as:

$$\dot{m} = \rho_e MR \tag{18}$$

The droplet diameter immediately before detachment, D_{dbd}, is determined by numerically solving the equation [4]:

$$F_T(D_{dbd}, I) - F_s(I) = 0 \tag{19}$$

The equation given above was solved as a one-dimensional root-finding problem over the droplet radius interval $r_d \in [1.001 r_e, 6 r_e]$. This equation represents the basic condition for estimating the droplet size immediately before detachment. In this equation, the total force F_T is calculated as the sum of the gravitational, electromagnetic, drag, and momentum flux forces, while the surface tension force is calculated using the effective neck radius.

After determining D_{dbd}, the droplet mass immediately before detachment is calculated as [4]:

$$m_{dbd} = \frac{4}{3}\pi\rho_e \left(\frac{D_{dbd}}{2}\right)^3 \tag{20}$$

A portion of the molten mass remains at the electrode tip after detachment. This residual mass is modelled by the expression:

$$m_{dr} = \frac{1}{2} m_{dbd} \left[1 + \frac{1}{1+\exp[-(k_4 + k_5 I)]}\right] \tag{21}$$

The mass of the detached droplet is:

$$m_{dd} = m_{dbd} - m_{dr} \tag{22}$$

Based on the mass of the detached droplet, its diameter is determined as:

$$D_{dd} = 2\left(\frac{3 m_{dd}}{4\pi\rho_e}\right)^{1/3} \tag{23}$$

The mean droplet detachment frequency is calculated from the ratio between the mass flow rate of the molten metal and the mass of the detached droplet:

$$f_d = \frac{\rho_e MR}{m_{dd}} \tag{24}$$

In this paper, the normalized droplet diameter immediately before detachment D_{dbd}/d_w is used as the main quantity for controlling the metal transfer mode, where $d_w = 2r_e$. The quantities D_{dd} and f_d are used as additional output indicators for interpreting the Pareto solutions.

2.4. Formulation of the Three-Objective Optimization Problem

The optimization variables are the welding current and the electrode wire extension length:

$$\mathbf{x} = [I, l_e] \tag{25}$$

The following ranges of the optimization variables were used in this paper:

$$180 \text{ A} \le I \le 270 \text{ A};\ 18 \text{ mm} \le l_e \le 30 \text{ mm} \tag{26}$$

The first objective function refers to the maximization of the melting rate. Since the multi-objective genetic algorithm solves a minimization problem, the maximization of the melting rate is transformed into the minimization of the negative normalized value:

$$f_1^0 = -\frac{MR}{MR_{ref}} \tag{27}$$

The second objective function defines the deviation of the normalized droplet diameter immediately before detachment from the target value:

$$f_2^0 = \left[\frac{\left(\frac{D_{dbd}}{d_w}\right)-\left(\frac{D_{dbd}}{d_w}\right)_{target}}{\left(\frac{D_{dbd}}{d_w}\right)_{target}}\right]^2 \tag{28}$$

In this paper, the following target value was adopted [4]:

$$\left(\frac{D_{dbd}}{d_w}\right)_{target} = 1.20 \tag{29}$$

The third objective function is introduced as a normalized Joule/stick-out index:

$$f_3^0 = \frac{I^2 l_e}{I_{max}^2 l_{e,max}} \tag{30}$$

This quantity is dimensionless and represents an indicator of resistive heating of the electrode wire extension. It does not represent the total heat input into the base material, but rather an additional criterion used to limit an excessive increase in the welding current and electrode wire extension length.

The relative error of the normalized droplet diameter is defined as:

$$\varepsilon_D = \frac{\frac{D_{dbd}}{d_w}-1.20}{1.20} \cdot 100\ \% \tag{31}$$

A penalty term was introduced into the optimization model for solutions that fall outside the desired projected/transitional region. First, the ratio between the momentum flux force and the electromagnetic force is defined:

$$R_F = \frac{F_{mf}}{|F_{em}|} \tag{32}$$

The penalty term can then be written as:

$$p_{proj} = w_{proj}\left[\max\left(0, R_{F,min} - R_F\right)^2 + \max\left(0, D_{min} - \frac{D_{dbd}}{d_w}\right)^2 + \max\left(0, \frac{D_{dbd}}{d_w} - D_{max}\right)^2\right] \tag{33}$$

where the following values were used in the numerical model: $R_{F,min} = 1, D_{min} = 1.00, D_{max} = 1.30$.

The active objective functions passed to the multi-objective genetic algorithm are therefore:

$$\begin{aligned} f_1 &= f_1^0 + p_{proj} \\ f_2 &= f_2^0 + p_{proj} \\ f_3 &= f_3^0 + p_{proj} \end{aligned} \tag{34}$$

The multi-objective optimization problem can be written in the form:

$$\min_{\mathbf{x}} \mathbf{f}(\mathbf{x}) = \min_{I,l_e}[f_1(I,l_e), f_2(I,l_e), f_3(I,l_e)] \tag{35}$$

with the defined bounds for I and l_e.

For each candidate pair (I, l_e), the model first calculates the effective neck radius and then determines D_{dbd} by solving (19). The obtained droplet size is used to calculate the detached droplet diameter, detachment frequency, objective functions, and penalty term. The resulting objective vector is used in the multi-objective genetic algorithm, while the dynamic layer is applied afterwards only for diagnostic verification of selected Pareto solutions.

Stricter conditions were used to identify the recommended operating window:

$$|\varepsilon_D| \leq 3\ \%;\ \frac{F_{mf}}{|F_{em}|} \geq 1;\ 1.15 \leq \frac{D_{dbd}}{d_w} \leq 1.25 \tag{36}$$

Characteristic solutions are then selected from the Pareto set: the maximum productivity solution, the target droplet solution, the minimum Joule/stick-out index solution, the three-objective compromise solution, and the recommended operating window solution.

To select the compromise solution from the Pareto set, the method of the closest point to the ideal point in the normalized objective space was used. Since all three objective functions are minimization functions, the ideal point after normalization has the coordinates $[0; 0; 0]$. For each Pareto solution i, $\min - \max$ normalization of each objective function is first performed:

$$f_{n,k}^{(i)} = \frac{f_k^{(i)} - \min(f_k)}{\max(f_k) - \min(f_k)} \tag{37}$$

The Euclidean distance from the ideal point is then calculated:

$$S_i = \sqrt{\left(f_{n,1}^{(i)}\right)^2 + \left(f_{n,2}^{(i)}\right)^2 + \left(f_{n,3}^{(i)}\right)^2} \tag{38}$$

The compromise solution is defined as:

$$i_{comp} = \arg\min_i S_i \tag{39}$$

The recommended solution within the operating window is selected using the same criterion, but only among the Pareto solutions that satisfy the conditions given in (36), therefore:

$$i_{OW} = \arg\min_{i \in OW} S_i \tag{40}$$

This procedure is not a curvature-based knee point method, but a normalized ideal-point compromise selection. However, in practical terms, it identifies a solution that represents a good balance between productivity, the target droplet size, and the Joule/stick-out index.

2.5. Dynamic Diagnostic Layer for Droplet Growth and Detachment

In addition to the static force-balance calculation, a dynamic diagnostic layer was introduced. This layer does not participate in the objective functions, but is used to verify the regularity of droplet growth and detachment for the selected Pareto solutions. The droplet is described as a variable-mass spring-damper system [5]:

$$m(t)\ddot{y}(t) + b\dot{y}(t) + k(t)y(t) = F_T(t) \tag{41}$$

where $y(t)$ is displacement of the droplet and b is linear damping coefficient.

The droplet mass increases due to the inflow of molten metal:

$$m(t+\Delta t) = m(t) + \dot{m}\Delta t \tag{42}$$

The instantaneous droplet radius is determined from the instantaneous mass:

$$r_d(t) = \left[\frac{3m(t)}{4\pi\rho_e}\right]^{1/3} \tag{43}$$

while the instantaneous droplet diameter is:

$$D_d(t) = 2r_d(t) \tag{44}$$

At each time step, the MFBM forces are recalculated using the instantaneous droplet diameter $D_d(t)$.

The effective stiffness of the system changes with the droplet mass:

$$k(t) = \max[k_{min}, k_0 + c_k(m(t) - m_0)] \tag{45}$$

The coefficient describing the change in stiffness with mass is defined as:

$$c_k = \frac{\dot{k}_{ref}}{\dot{m}_{ref}} \tag{46}$$

where the reference mass flow rate is:

$$\dot{m}_{ref} = \rho_e\left(c_1 I_{ref} + c_2 \rho_{res} I_{ref}^2 l_{e,ref}\right) \tag{47}$$

Droplet detachment is assumed to occur when the MFBM force-balance condition defined in (2) is satisfied.

After detachment, the mass is reset to the residual mass [4]:

$$m_{res} = \frac{1}{2} m(t_{det}) \left[1 + \frac{1}{1+\exp[-(k_4 + k_5 I)]}\right] \tag{48}$$

The dynamic layer is used only as a diagnostic tool and not as an active optimization criterion. This use of the dynamic layer is based on the concept of modelling the droplet as a lumped-parameter system, which has been used in the literature for the analysis of oscillations, resonant behavior, and metal transfer stability [5], [8].

The main model constants and coefficients used in the numerical analysis are summarized in Table 1.

Table 1: Main model constants and coefficients used in the numerical analysis [1], [4,5]

r_e	ρ_e	g	μ_0	C_d	ρ_p	v_p	γ	c_1	c_2	ρ_{res}	k_4
0.6	7860	9.81	$4\pi \cdot 10^{-7}$	0.44	1.784	10	1.3	$3.3 \cdot 10^{-10}$	$0.78 \cdot 10^{-10}$	0.43	-0.364
mm	$\mathrm{kg/m^3}$	$\mathrm{m/s^2}$	H/m	–	$\mathrm{kg/m^3}$	m/s	N/m	$\mathrm{m^3/(sA)}$	$\mathrm{m^3/(s\Omega A^2)}$	Ω/m	–
k_5	MR_{ref}	I_{max}	$l_{e,max}$	w_{proj}	b	k_{min}	k_0	$\dot{k}_{ref}$	m_0	I_{ref}	$l_{e,ref}$
0.0062	10^{-7}	270	30	1.0	$3 \cdot 10^{-4}$	0.01	0.2	-0.8	$5.0 \cdot 10^{-7}$	200	20
$\mathrm{A^{-1}}$	$\mathrm{m^3/s}$	A	mm	–	Ns/m	N/m	N/m	N/(ms)	kg	A	mm

3. RESULTS AND DISCUSSION

The optimization was performed for a welding current range of 180 to 270 A and an electrode wire extension length range of 18 to 30 mm. The target value of the normalized droplet diameter immediately before detachment was $D_{dbd}/d_w = 1.20$. The multi-objective genetic algorithm was run with a population size of 60 for 60 generations. After duplicate removal using tolerances of 0.02 A for current and 0.02 mm for electrode wire extension length, 22 Pareto-optimal solutions were retained. The obtained Pareto set shows a compromise between three requirements: increasing the melting rate, maintaining the target droplet size, and reducing the normalized Joule/stick-out index.

Figure 2 shows the Pareto front in the space of the three active objective functions. The three-dimensional distribution confirms the absence of a single dominant solution. The solutions with the highest productivity are located at higher values of welding current and electrode wire extension length, but at the same time they have a higher value of the third objective function and a lower D_{dbd}/d_w ratio. In contrast, the solutions with a lower Joule/stick-out index have lower productivity and, in some cases, produce droplets larger than the target value. This confirms that the selection of process parameters cannot be based solely on maximizing the melting rate, but must also include droplet size control and limitation of the thermal loading of the electrode wire extension.

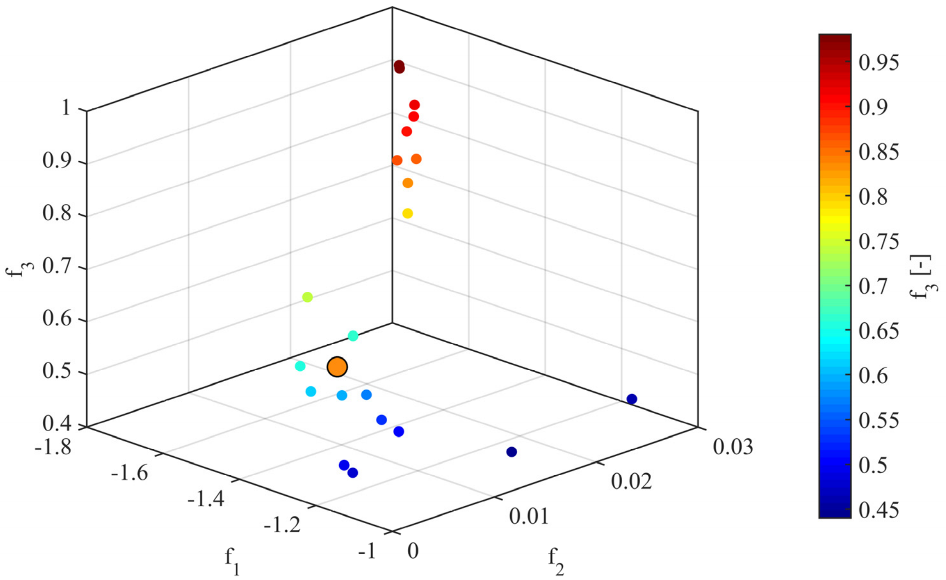

Figure 2: Pareto front in the space of three active objectives

The map of the normalized droplet diameter in the $I - l_e$ space, shown in Figure 3, indicates that the value of D_{dbd}/d_w changes predominantly with the welding current. The contour corresponding to the target value ($D_{dbd}/d_w = 1.20$) is located in the region around 231 A, while the influence of the electrode wire extension length is less pronounced. On the other hand, the melting rate map, given in Figure 4, shows that MR increases with both increasing current and increasing electrode wire extension length. Therefore, the solutions with the highest productivity are located close to the upper boundary of the analyzed space; however, such solutions deviate from the target droplet size and have an increased Joule/stick-out index.

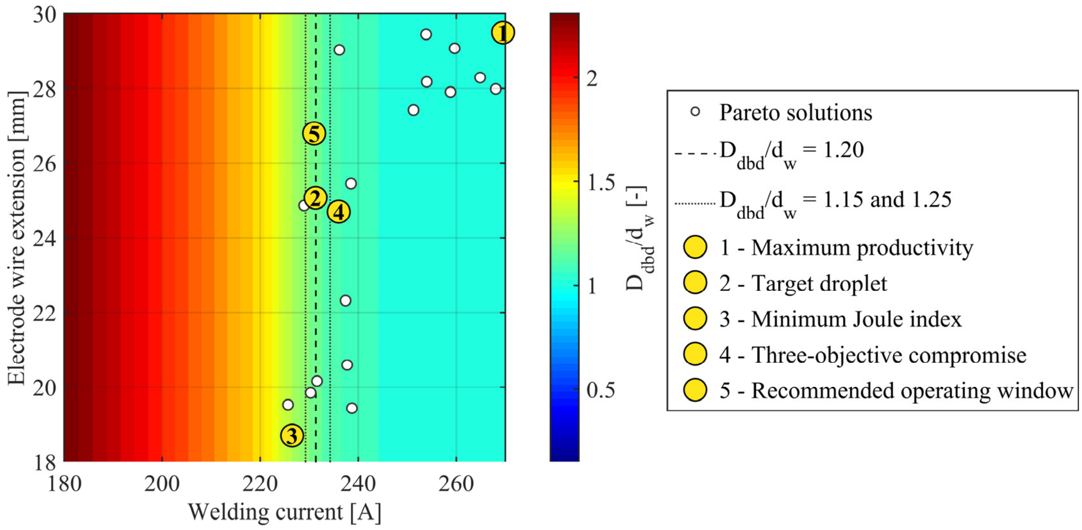

Figure 3: Map of the $I - l_e$ space with contours of D_{dbd}/d_w

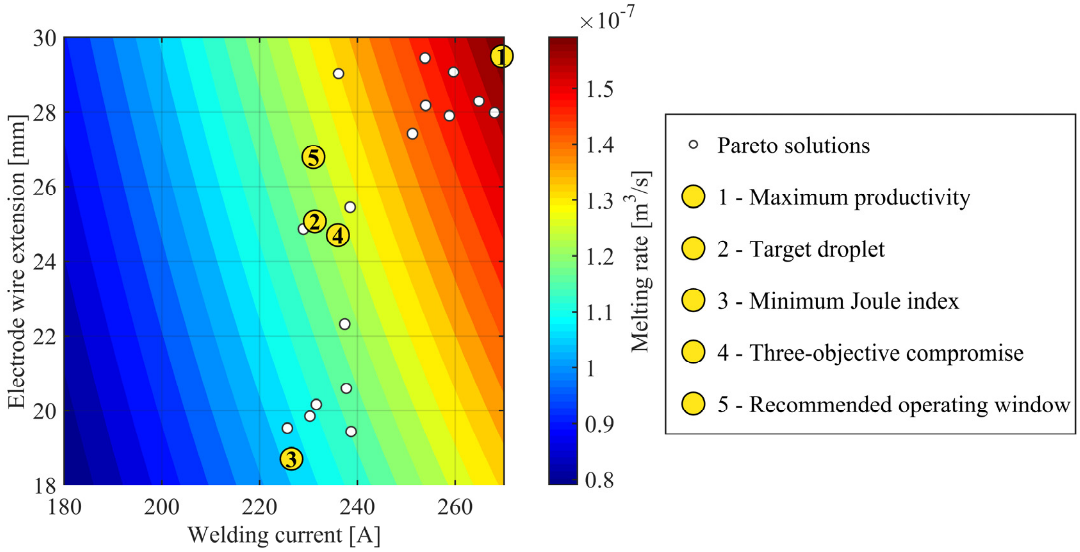

Figure 4: Map of the $I - l_e$ space with contours of melting rate

The map of the normalized Joule/stick-out index f_3, shown in Figure 5, indicates the expected increase in this quantity with increasing welding current and electrode wire extension length. This result confirms the role of the third objective function as an additional constraint that prevents the selection of solutions with excessive resistive heating of the electrode wire extension. Therefore, the maximum productivity solutions, although they provide the highest melting rate, are not necessarily the most favorable from the standpoint of the overall compromise between all three objectives.

This trend is consistent with the known behavior of metal transfer in the GMAW process: increasing the current generally reduces the droplet size and increases the transfer frequency, while the electrode wire extension length affects the melting rate and the thermal state of the electrode [1,2]. Kang and Chung further showed that, above the transition current, the tapering of the electrode tip reduces the surface-tension effect and increases the relative influence of electromagnetic forces, which supports the need to account for both droplet size and force balance in the model [6].

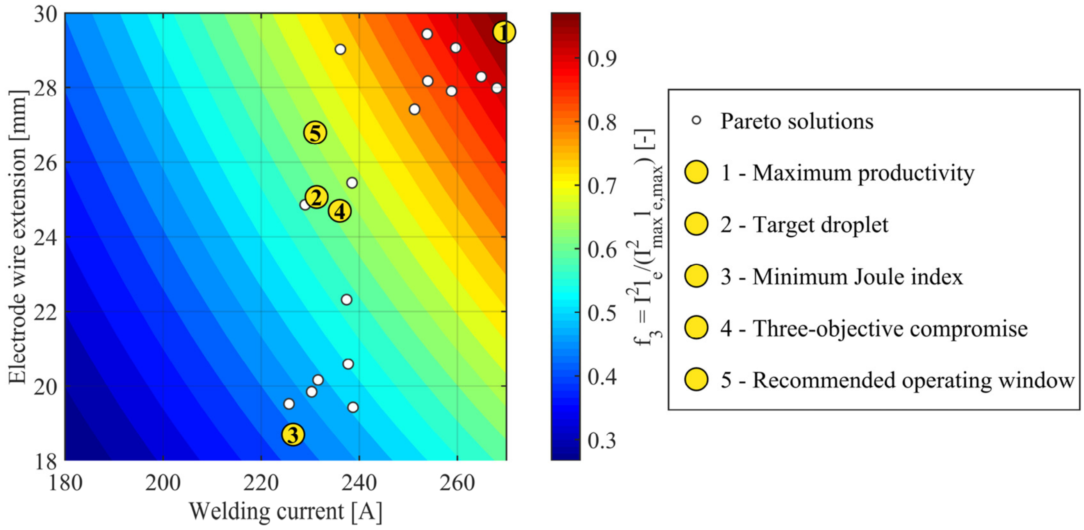

Figure 5: Map of the $I - l_e$ space with contours of f_3

Five representative solutions were selected from the Pareto set: the maximum productivity solution, the target droplet solution, the minimum Joule/stick-out index solution, the compromise solution, and the solution within the recommended operating window. Their values are presented in Table 2. The target droplet solution shows the best agreement with the prescribed value ($D_{dbd}/d_w = 1.20$), while the maximum productivity solution represents the upper limit of MR, but with a clear trade-off in droplet size and Joule/stick-out index. The solution with the minimum Joule/stick-out index has the lowest thermal loading of the electrode wire extension, but produces a droplet larger than the target value. The compromise solution represents a balanced choice in the three-objective space, while the solution within the recommended operating window maintains the droplet size close to the target value with slightly higher productivity compared with the strict target droplet solution.

Table 2: Representative Pareto solutions

Solution	I [A]	l_e [mm]	$\frac{D_{dbd}}{d_w}$ [−]	ε_D [%]	$MR \cdot 10^{-7}$ [m^3/s]	f_d [Hz]	f_3 [−]
Max. productivity	269.6	29.5	1.02	−15.32	1.61	1590.8	0.98
Target droplet	231.3	25.1	1.2	−0.01	1.21	607.8	0.61
Min. Joule index	226.5	18.7	1.34	11.37	1.07	379.4	0.44
Three-obj. comprom.	236.0	24.7	1.13	−6.01	1.24	764.7	0.63
Recom. oper. window	231.0	26.8	1.21	0.50	1.24	612.0	0.65

The force contribution analysis, shown in Figure 6, indicates that the electromagnetic force (F_{em}) and the momentum flux force (F_{mf}) are dominant in the representative solutions. The gravitational force (F_g) and the drag force (F_d) have a considerably smaller contribution to the total detaching force. This force relationship confirms the suitability of the MFBM model in the analyzed region, since the inclusion of the momentum flux force represents the key difference compared with the classical force balance model. At higher currents, the influence of electromagnetic effects increases, leading to a reduction in droplet size and an increase in detachment frequency.

The recommended operating window is shown in Figure 7. This representation shows that the operating window is located within a relatively narrow current range, close to the contour corresponding to the target value of the normalized droplet diameter. Most of the high-productivity Pareto solutions are located outside the recommended operating window, because they do not simultaneously satisfy the conditions related to proximity to the target droplet size and the constraints defined through the force ratio $R = F_{mf}/|F_{em}|$. Therefore, the solution within the recommended operating window can be considered the most favorable practical choice when the priority is a stable and controlled droplet size with acceptable productivity. Figure 8 shows the selection of the compromise solution in the normalized objective space. The selected solution has the smallest Euclidean distance from the ideal point and therefore represents a balanced trade-off between productivity, droplet size, and the Joule/stick-out index, rather than an extreme solution with respect to a single objective.

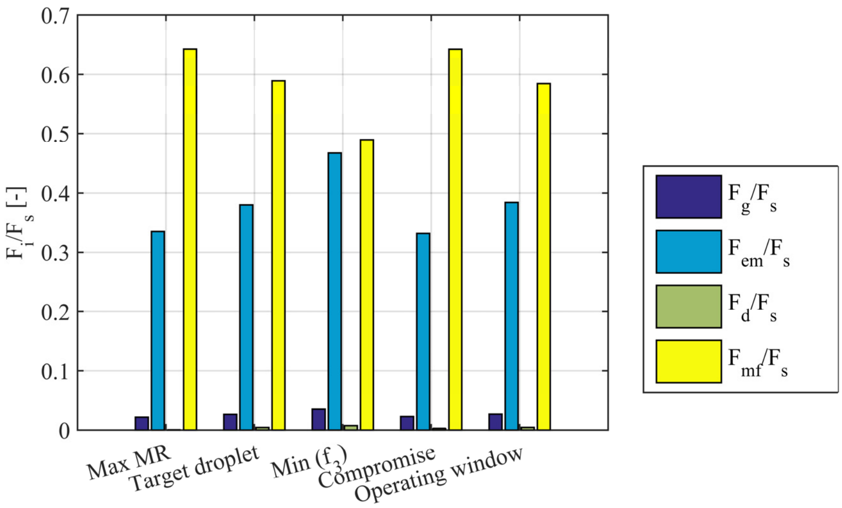

Figure 6: Force contributions for representative Pareto solutions

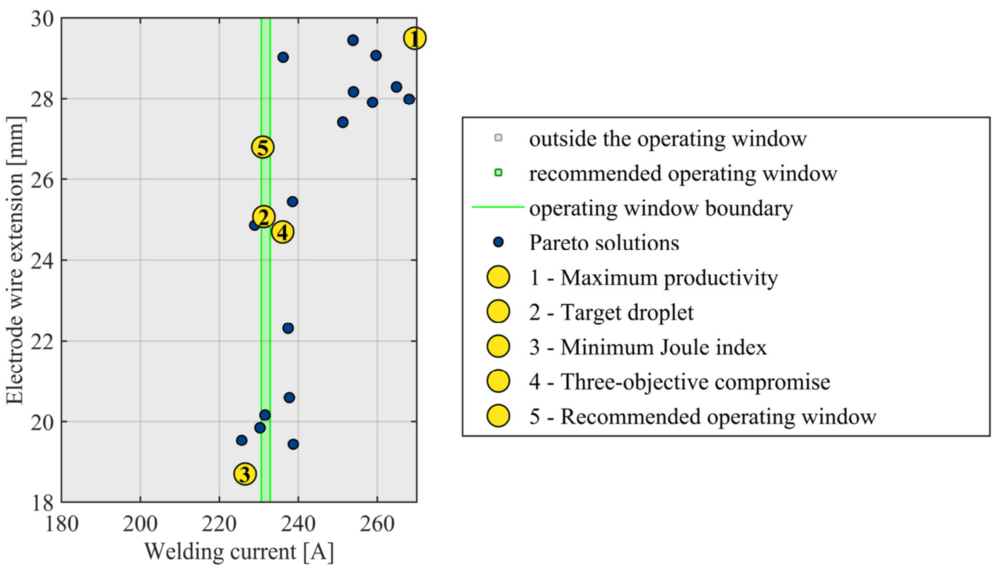

Figure 7: Recommended operating window and Pareto solutions

An additional verification of the selected solutions was performed using the dynamic diagnostic layer. The simulation was carried out for a total simulation time of $T_{sim} = 0.5$ s, with a time step of $\Delta t = 5 \cdot 10^{-5}$s as recommended in [4].

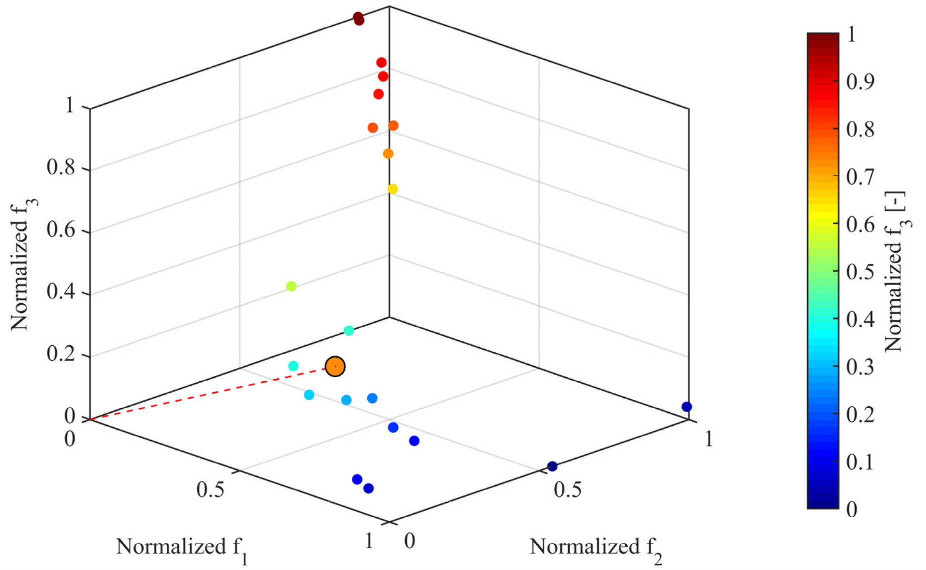

Figure 8: Compromise solution in the normalized three-objective space

The time variation of the droplet diameter for the compromise solution, shown in Figure 9, indicates the repetition of the growth and detachment cycle. After the condition defined by the MFBM criterion is reached, the droplet detaches, the mass is reset to the residual value, and a new cycle begins. The time variation of the forces for the compromise solution, shown in Figure 10, indicates the periodic approach of the total detaching force to the surface tension force, confirming the consistency of the implemented detachment condition. The repetition of the growth, detachment, and mass-reset cycles indicates regular behavior of the selected solutions within the introduced diagnostic model.

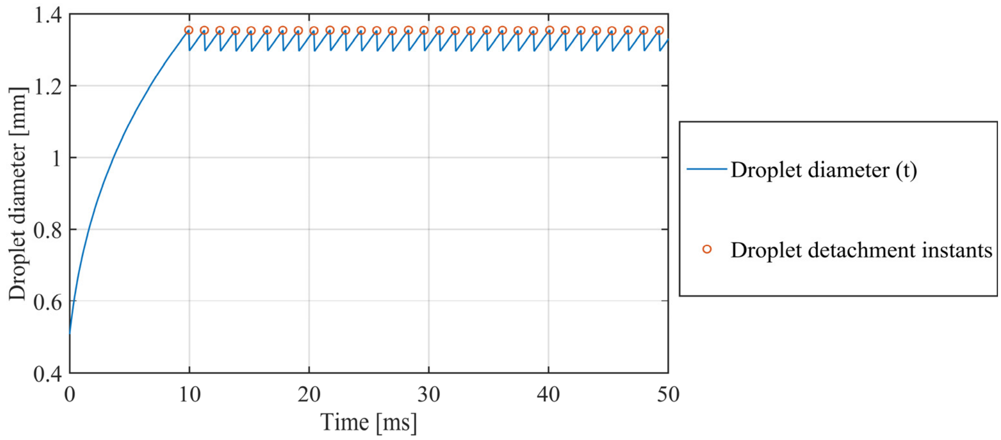

Figure 9: Time variation of the droplet diameter in the MFBM diagnostic layer

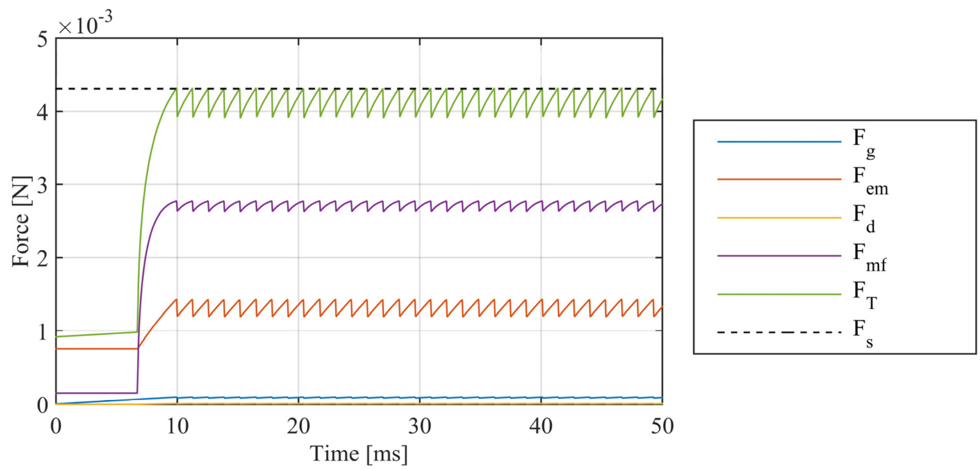

Figure 10: Time variation of forces in the MFBM diagnostic layer

Based on the obtained results, it can be concluded that the most favorable region for achieving the target droplet size is located around $I \approx 231$ A. Increasing the electrode wire extension length in this region enables an increase in the melting rate, but with a moderate increase in the Joule/stick-out index. Therefore, the recommended operating window solution at $I = 231.0$ A and $l_e = 26.8$ mm is identified as the most favorable practical solution, because it simultaneously satisfies the condition of proximity to the target droplet size, provides higher productivity than the strict target solution, and remains within an acceptable range of the third objective function.

4. CONCLUSIONS

In this paper, a three-objective optimization model was developed for the preliminary selection of welding current and electrode wire extension length in the GMAW process. The model is based on a modified force balance model (MFBM), in which droplet detachment is determined from the equilibrium condition between the total detaching force and the surface tension force. Compared with the basic MFBM model, a pressure-balance correction of the effective electrode wire neck radius was introduced to account for the influence of the tapering/necking effect at higher current values.

The optimization variables were the welding current I and the electrode wire extension length l_e, while the objective functions were defined to simultaneously maximize the melting rate, minimize the deviation of the normalized droplet diameter immediately before detachment from the target value, and minimize the normalized Joule/stick-out index. The obtained Pareto set, consisting of 22 non-duplicate solutions, shows a clear compromise between productivity, droplet size control, and thermal loading of the electrode wire extension.

The solution within the recommended operating window represents the most favorable practical choice, because it maintains the droplet size close to the target value while providing slightly higher productivity compared with the strict target droplet solution. The force contribution analysis showed that the electromagnetic force and the momentum flux force dominate in the representative solutions, while the gravitational force and the drag force are considerably smaller, confirming the suitability of the MFBM model in the analyzed projected/transitional metal transfer region.

The dynamic diagnostic layer showed regular droplet growth and detachment cycles for the selected Pareto solutions, while being used only as an additional verification tool and not as an active optimization criterion. The proposed model therefore represents a numerically efficient and physically interpretable approach for preliminary GMAW parameter selection. Future work should include experimental validation using high-speed imaging, current and voltage measurements, and comparison of the calculated droplet size and detachment frequency with experimental data.

ACKNOWLEDGEMENTS

The authors express their gratitude to the Ministry of Science, Technological Development and Innovation of the Republic of Serbia for supporting this research (Contract Nos. 451-03-33/2026-03/200108 and 451-03-34/2026-03/200108). This research contributes to the United Nations 2030 Agenda for Sustainable Development, specifically to Sustainable Development Goal 9: Build resilient infrastructure, promote inclusive and sustainable industrialization and foster innovation.

REFERENCES

[1] Y-S. Kim and T. W. Eagar, "Analysis of metal transfer in gas metal arc welding", Welding Journal, Vol. 72, pp. 269-278, (1993)

[2] M. S. Węglowski, Y. Huang, and Y. M. Zhang, "An investigation of metal transfer process in GMAW, Engineering Transactions, Vol. 56(4), pp. 345-362, https://doi.org/10.24423/ENGTRANS.189.2008, (2008)

[3] E. Uddin, U. Iqbal, N. Arif, and S. R. Shah, "Analysis of metal transfer in gas metal arc welding", AIP Conference Proceedings, 24 July 2019, https://doi.org/10.1063/1.5114003, (2019)

[4] M. M. Anzehaee and M. Haeri, "Estimation and control of droplet size and frequency in projected spray mode of a gas metal arc welding (GMAW) process", ISA Transactions, Vol. 50(3), pp. 409-418, https://doi.org/10.1016/j.isatra.2011.02.004, (2011)

[5] U. Ersoy, E. Kannatey-Asibu, and S. J. Hu, "Analytical modeling of metal transfer for GMAW in the globular mode", Journal of Manufacturing Science and Engineering, Vol. 130(6), pp. 91-98, https://doi.org/10.1115/1.3006317, (2008)

[6] M. S. Kang and H. Chung, "Dynamic force balance model considering tapering effect in gas metal arc welding", Journal of Materials Processing Technology, Vol. 257, pp. 79-87, https://doi.org/10.1016/j.jmatprotec.2018.02.029, (2018)

[7] J. S. Thomsen, "Advanced control methods for optimization of arc welding", PhD Thesis, Aalborg University (Denmark), (2004)

[8] X. Zhang, H. Gao, and G. Zhang, "Current-independent metal transfer by utilizing droplet resonance in gas metal arc welding", Journal of Materials Processing Technology, Vol. 279(17), https://doi.org/10.1016/j.jmatprotec.2019.116571, (2020)